Accepted manuscript *Environmental Modeling & Software*
https://doi.org/10.1016/j.envsoft.2023.105768

The Effects of Digital Elevation Model Resolution on the PyFLOWGO Thermorheological Lava Flow Model

Ian T. W. Flynn[1], Magdalena O. Chevrel[2,3,4], David A. Crown[5], and Michael S. Ramsey[1]

[1]Department of Geology and Environmental Science, University of Pittsburgh, Pittsburgh, PA, USA.
[2]Laboratoire Magmas et Volcans (LMV), Université Clermont Auvergne, CNRS, IRD, OPGC, 63000 Clermont-Ferrand, France.
[3]Observatoire Volcanologique du Piton de la Fournaise, Institut de Physique du Globe de Paris, 97418 La Plaine des Cafres, France.
[4]Université Paris Cité, Institut de Physique du Globe de Paris, CNRS, 75005 Paris, France.
[5]Planetary Science Institute, Tucson, AZ, USA.

Corresponding author: Ian Flynn (itf2@pitt.edu)

Highlights:

- We present a topographic sensitivity analysis for the PyFLOWGO lava flow model.
- Examined DEM resolutions were based on common Earth and planetary datasets.
- A model step size equal to or smaller than the DEM resolution should be used.
- DEM resolution has a quantifiable impact on the modeled flow length (up to 35%).

Abstract (150/150 word limit)

Topography is a fundamental factor influencing the emplacement of lava flows. We assess the impact of topographic resolution on the thermorheological PyFLOWGO model, specifically with digital elevation model (DEM) resolutions commonly available for Earth and other planetary bodies where flow modeling is relevant. We examined PyFLOWGO output parameters (e.g., channel length, core temperature, and flow velocity) to assess model sensitivity to topography in order to document model uncertainties and optimize future application. This study uses rheologic and topographic data from the Tolbachik, Russia 2012-2013 eruption as model constraints. Using moderate to lower resolution topographic data overestimates the channelized flow length by up to 35% due to differences in the distribution of slopes topographic variability at different resolutions and resulting effects on the modeled lava velocity down channel. Determining the impact of topography on thermorheological lava flow models such as PyFLOWGO is important to correctly interpret the results for channelized flows.

Keywords: FLOWGO, Sensitivity analysis, Planetary science, Volcanology, Volcanic eruption, Tolbachik, Topography, DEM

1 Introduction

The emplacement of a lava flow is controlled by a number of factors, such as the rheology (i.e., lava viscosity, which depends on eruption temperature, composition, and degree of crystallization), the effusion rate, external environmental conditions (i.e., gravity, atmospheric density, and temperature), and importantly, the topography over which it flows. Modeling lava flow emplacement attempts to simplify these conditions to address specific volcanological questions. For lava flows on Earth, modeling is commonly performed either once the flow is emplaced in order to determine the rheological parameters or eruptive conditions (e.g., Harris & Rowland, 2001; Ramsey et al., 2019; Rowland et al., 2005) or in a prognostic manner for hazard response and assessment (e.g., Chevrel et al., 2022; Favalli et al., 2005, 2012; Harris & Rowland, 2015). For investigations of inactive/older flows on Earth and other planetary bodies, the goal is typically to determine the eruption conditions and lava rheology necessary to produce the observed

flow length or area (e.g., Flynn et al., 2022; Ganci et al., 2020; Peters et al., 2021). No matter how a lava flow model is applied, or the level of complexity included, topography is an essential dataset. Therefore, understanding how the spatial resolution of a topographic dataset affects model results is critical.

For modeling recent terrestrial flows, it is common to have access to digital elevation models (DEM) of the pre-flow surface ranging from moderate (~10-50 m/pixel) to high (≤10 m/pixel) resolution that are derived from photogrammetry, LIDAR, or InSAR datasets (Table 1) (e.g., Chevrel et al., 2021; Kubanek et al., 2015; Richardson & Karlstrom, 2019). However, pre-flow topography is not available for investigations of older lava flows. Some planetary bodies may have limited coverage of high to moderate resolution DEMs of a study region, whereas others are limited to much lower resolution DEMs (Table 1). The resolution of planetary DEMs and lack of pre-flow datasets have resulted in many studies using a constant slope to perform lava flow modeling (e.g., Baloga & Glaze, 2008; Hiesinger et al., 2007; Peters et al., 2021). However, several previous studies concluded that variations in local topography have a measurable impact on model results of a lava flow's emplacement (Glaze & Baloga, 2007; Russo et al., 2022).

Table 1: DEM datasets commonly available for Earth, Mars, and Venus.

Planetary Body	Instrument	Spatial Resolution	Global Surface Coverage (%)	References
Earth	ASTER[a]	30 m/pixel	100%	(Hirano et al., 2003)
	SRTM[b]	30 m/pixel	100%	(Farr et al., 2007)
	InSAR	12 m/pixel	~97%	(Rizzoli et al., 2017)
	ArcticDEM	2 m/pixel	~23%	(Takaku et al., 2020)
Mars	MOLA[c]	463 m/pixel	100%	(Zuber et al., 1992)
	MOLA/HRSC[d]	200 m/pixel	100%	(Fergason et al., 2018)
	HRSC	50 m/pixel	~44%	(Jaumann et al., 2007)
	CTX[e]	~20 m/pixel	~17%	(Breton et al., 2019)
	HiRISE[f]	~1-2 m/pixel	~0.4%	(Sutton et al., 2022)
Venus	Altimeter	10-20 km/pixel	98%	(Ford & Pettengill, 1992)
	SAR Stereo	1-2 km/pixel	20%	(Herrick et al., 2012)

[a] Advanced Spaceborne Thermal Emission and Reflection radiometer

[b] Shuttle Radar Topography Mission

[c] Mars Orbiting Laser Altimeter

[e] Context Camera

[f] High Resolution Imaging Experiment

There are numerous lava flow emplacement models, and many have associated sensitivity analyses to topography, including DOWNFLOW (Favalli et al., 2011), MAGFLOW (Bilotta et al., 2019), MULTIFLOW (Richardson & Karlstrom, 2019), and Q-LAVHA (Mossoux et al., 2016). However, this has not been done for FLOWGO/PyFLOWGO (Chevrel et al., 2018; Harris & Rowland, 2001). The focus of this study, therefore, is to investigate the impact of topographic data resolution on the FLOWGO thermorheological model's output with specific focus on commonly available DEM resolutions for Earth and other planetary bodies. We use a terrestrial study case that was presented in Ramsey et al. (2019): the 2012-2013 Tolbachik eruption (Figure 1). It was chosen because Ramsey et al. (2019) already performed the FLOWGO modeling and provided the input rheological parameters that best fit the lava flow.

1.1 The 2012-2013 Tolbachik Eruption

The Tolbachik volcanic complex is one of three active volcanoes (Klyuchevskoy, Bezymianny, and Tolbachik) that make up the Klyuchevskoy Volcano Group (KVG) in Kamchatka (Russia). Tolbachik is comprised of two stratovolcanoes, Ostry and Plosky Tolbachik, with multiple cones and lava flows to the south (Figure 1).

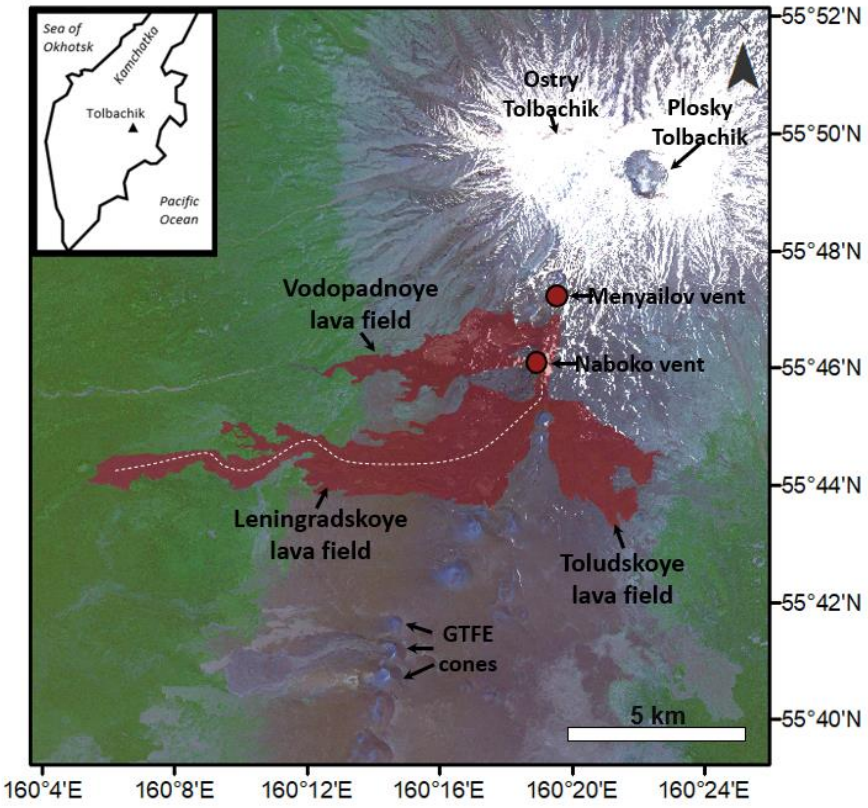

Figure 1. The Tolbachik volcanic complex comprised of Ostry and Plosky Tolbachik. To the immediate south of the volcanic complex, are the three flow fields (shown in red) and two vents (red circles with black outline) formed during the 2013 Tolbachik Fissure Eruption (TFE-50). Further south are three cones formed during the Great Tolbachik Fissure Eruption (GTFE). The white dashed line indicates the path of the central channel used for the PyFLOWGO model. Base image from Planets RapidEye Sensor (~5 m/pixel, visible), acquired on 18 June 2014.

Historically, the complex has produced eruptions throughout the Holocene and more recent times (Churikova et al., 2015). The two most notable eruptions from the complex are the 1975-1976 Great Tolbachik Fissure Eruption (GTFE) and the 2012-2013 Tolbachik Fissure Eruption (TFE-50), named after the 50th anniversary of the Institute of Volcanology and Seismology. During the GTFE new monogenetic cones and several associated lava flows were emplaced along the southern slope of Plosky Tolbachik (Figure 1) (Fedotov et al., 1984). However, most of the deposited material is pyroclastic, infilling the area around the cones. The smaller TFE-50 eruption produced mainly lava flows originating from vents that formed monogenetic cones closer to the main volcanic edifice and along the same path that produced the GTFE (Churikova et al., 2015).

During the TFE-50 eruption, which began on 27 November 2012, both Hawaiian and Strombolian eruption styles occurred, producing basaltic trachyandesite lava flows (Belousov &

Belousova, 2017). The average effusion rate, measured with aerial photogrammetric surveys, early in the eruption was ~440 m^3/s, which gradually waned until the eruption ended on 5 September 2013 (Belousov & Belousova, 2017; Ramsey et al., 2019). At the end of the eruption three prominent flow fields had formed, Vodopadnoye, Leningradskoye, and Toludskoye (Figure 1). The Vodopadnoye flow field (area 6.17 km^2, volume 0.04 km^3) originated from the Menyailov vent and is comprised mostly of ʻaʻā flows (Belousov et al., 2015; Belousov & Belousova, 2017). Both the Leningradskoye (area 22.44 km^2, volume 0.35-0.39 km^3) and Toludskoye (area 8.4 km^2, volume 0.1 km^3) flow fields originated from the Naboko vent (Belousov et al., 2015). The Leningradskoye flow field contains mostly ʻaʻā and the Toludskoye contains ʻaʻā, pāhoehoe and various transitional lava types (Belousov et al., 2015; Belousov & Belousova, 2017). The total volume of lava produced from the TFE-50 eruption makes it one of the largest in history and one of the most thermally radiant eruptions in the modern satellite era (Ramsey et al., 2019). This study focuses specifically on the large, channelized lava flow that formed early in the eruption in the Leningradskoye flow field.

2. FLOWGO model

Lava flow modeling is a powerful tool for hazard mitigation and interpreting emplacement processes as well as understanding the evolution of thermorheological properties of flowing lava. One of the most extensive and widely utilized lava flow models is FLOWGO/PyFLOWGO (Table 2). The original FLOWGO model was recoded and updated in the Python scripting language to PyFLOWGO, which allows for improved iteration and customization (Chevrel et al., 2018). For all modeling discussed throughout the rest of the manuscript, PyFLOWGO is used. As of 2023, twenty-two peer-reviewed publications have used FLOWGO or PyFLOWGO to investigate both active and inactive lava flows on Earth at a variety of locations. It has also been utilized to investigate volcanism on four other planetary bodies (Table 2).

Table 2. Examples of studies employing FLOWGO/PyFLOWGO

Study Locations	References
Earth	
Cameroon	(Wantim et al., 2013)
D.R. Congo	(Mossoux et al., 2016)
Galapagos	(Rowland et al., 2003)
Hawai'i	(Chevrel et al., 2018; Harris et al., 2022; Harris & Rowland, 2015, 2001; Mossoux et al., 2016; Riker et al., 2009; Robert et al., 2014; Rowland et al., 2005; Thompson & Ramsey, 2021)
Italy	(Harris et al., 2007, 2011; Wright et al., 2008)
Kamchatka	(Ramsey et al., 2019)
La Reunion	(Chevrel et al., 2018, 2022; Harris et al., 2016, 2019; Peltier et al., 2022; Rhéty et al., 2017)
Planetary	
Mars	(Flynn et al., 2022; Rowland et al., 2004)
Mercury	(Vetere et al., 2017)
Moon	(Lev et al., 2021)
Venus	(Flynn et al., 2023)

FLOWGO, originally described in Harris and Rowland (2001) is a one-dimensional, thermorheological model applicable to open channelized flows. It calculates the thermal budget and resulting lava properties (i.e., core and surface temperature, and crystallinity) of a lava volume down channel at each pre-defined interval step. At each step, the resulting depth-averaged viscosity and velocity are obtained. The model is only applicable for cooling-limited flows and to the well-established channel region, and not the dispersed flow region that extends downslope beyond the channel. For flows on Earth, the dispersed zone may be a region up to ~3 km beyond the end of the channel (Dietterich & Cashman, 2014; Harris et al., 2022; Lipman & Banks, 1987). For channelized flows on Mars, the dispersed zone may be up to ~49 km long (Flynn et al., 2022).

Thermal budgeting includes the radiative (Q_{rad}) heat loss from the flow surface, convective (Q_{conv}) heat loss to the atmosphere, conductive (Q_{cond}) heat loss to the channel walls and floor, and heat loss due to vaporization of precipitation (Q_{rain}) (where applicable). The heat gains are due to latent heat of crystallization (Q_{cryst}) and viscous dissipation (Q_{visc}) within the flowing lava. Under typical terrestrial conditions, heat loss from the modeled lava is dominated by radiative heat flux, which is a function of the temperature and effective emissivity of the lava's radiating surface (molten and crusted fractions) (Ramsey et al., 2019; Rowland et al., 2004).

PyFLOWGO makes five assumptions that define the model and where it is applicable. (1) The lava flow velocity is defined by the effusion rate, which is held constant downflow, in a channel with a defined depth and width (either estimated for an active flow or measured directly on an older flow) on a given slope. (2) The lava flow must be confined to an open channel with no continuous roofing or tube formation. (3) The vertical thermal structure of the lava is divided into three layers: a cooler basal crust, a homogeneous high-temperature molten core, and a radiating upper surface. (4) The model simulates the propagation of a channel-confined lava unhindered by the flow front or levee formation. (5) The flow is cooling- and not supply-limited.

As a cooling-limited flow slows down because of heat loss and increasing viscosity, it spreads laterally, commonly marking the end of the central channel, and will stop after it has cooled to an extent that its rheological behavior impedes forward motion (Chevrel et al., 2018). In practice, PyFLOWGO has one of three stopping conditions: (1) the modeled velocity reaches zero; (2) the modeled temperature of the flow core reaches the point of solidus; (3) the modeled yield strength of the flow core increases such that the flow is unable to advance. As the modeled velocity reaches zero the simulated channel width will increase substantially.

The main goal of this work is to investigate the effects of DEM resolution on PyFLOWGO's results. The rheologic input parameters are the same as provided by Ramsey et al. (2019) for the TFE-50 Leningradskoye channelized lava flow (Table 3), with the exception of the lava's thermal emissivity module. As shown by Ramsey et al. (2019) and later by Thompson and Ramsey (2021), PyFLOWGO is also sensitive to the assumed emissivity value chosen, with lava flow runout distance varying by ~6%. As part of this work, we also explore the effect of the three different emissivity modules (where emissivity is considered constant, bimodal, and a function of surface temperature) within PyFLOWGO and their effectiveness to reproduce the observed length of a lava channel for the TFE-50 eruption. Between the three emissivity module options there is a 700 m (~6%) difference in modeled channel length. Full details of this investigation can be found in the Supplemental Material. For the DEM analysis, we choose to use the variable emissivity option because, similar to Thompson and Ramsey (2021), it appears to most accurately reproduce a flow's emplacement compared to the other emissivity options in PyFLOWGO.

3 Methods: Topographic Study

Following the argument presented in Bilotta et al. (2019) for the MAGFLOW model, the resolution of a DEM has both a direct and a secondary impact on modeling. The direct impact is the resolution of the DEM, and the secondary impact is the model step size (i.e., how frequently the model accounts for changes in topography). Both models (MAGFLOW and PyFLOWGO) require topography and a step size. The model step size defines the distance (in meters) that the simulated lava advances per each model iteration. PyFLOWGO allows the user to define a step size that is independent of the DEM resolution. The influence of DEM resolution versus the model step size is investigated using a convergence analysis (see section 3.2).

PyFLOWGO does not directly intake a DEM profile. It requires a slope transect that follows the path of the lava flow's central channel. For each DEM resolution, a slope map was created using ArcGIS v10.7 and the "Slope" tool.

3.1 Topographic Data

To assess the impact that DEM resolution has on any lava flow emplacement model, numerous approaches are possible. For locations where multiple DEMs of different resolutions are available, comparing the model outputs of each is possible (Stefanescu et al., 2012). The generation of artificial terrain through Monte Carlo algorithms that control the variation and amount of noise/error is another approach (Richardson & Karlstrom, 2019). For this analysis, a deterministic approach similar to the method of Bilotta et al. (2019) was used. We used a high resolution (5 m) DEM as the baseline and derived multiple lower-resolution DEMs (10, 15, 20, 30, 50, 100 and 200 m) for comparison. It is important to note, however, that a DEM degraded to a lower resolution from a higher resolution DEM is not identical to a DEM produced at that same spatial resolution. However, for this study, the smaller-scale differences between these two approaches are not considered critical to the final model output.

The baseline topographic data pre-date the TFE-50 eruption and therefore represent the pre-flow topography. Colleagues (Viktor Dvigalo and Alexander Belousov) at the Institute of Volcanology and Seismology, Russia, generated the data necessary to produce the DEM using aerial images. The point cloud data provided were used to create the 5 m DEM with ArcGIS v10.7 and the "3D Analyst" toolbox, and the "Terrain to Raster" tool. This resolution was chosen because

it is similar to the DEMs produced from CubeSat data and photogrammetry (i.e., Planet Labs) (Ghuffar, 2018). The moderate and low resolution DEMs represent common scales from other remote sensing data (Table 1). Lastly, for comparison we performed simulations on a constant slope that is the average value obtained on the 5 m DEM (11.3° ± 0.11) flow path transect. Using a constant slope is relevant because this approximation is commonly used for planetary lava flow modeling (e.g., Baloga & Glaze, 2008; Garry et al., 2007; Peters et al., 2021).

3.2 Convergence Analysis

A necessary step for assessing a model is a numerical convergence analysis. For PyFLOWGO, a convergence analysis consists of varying the step size and assessing the value returned for the variables of interest. Stabilization of the variable of interest within an acceptable range determines whether the step size is sufficient. Step sizes were chosen to determine if there is any relation between the employed step size and the resolution of the DEM. We therefore tested step sizes of 1 m, 5 m, 10 m, 15 m, 30 m, 50 m, 100 m, and 200 m on the slope profiles extracted from the 5 m reference DEM and from the lower resolution DEMs with pixel size of 15 m, 30 m, 200 m, as well as the constant slope profile. To assess the convergence analysis, the maximum distance traveled by the channel and final lava core temperature are used. This convergence analysis is similar to the one performed by Chevrel et al. (2018).

4 Results

4.1 Effects of DEM resolution on slope values

PyFLOWGO does not directly use a DEM to initiate the model but rather a 1D slope profile that is derived from the DEM and drawn along the flow path. The elevation value of a pixel of the DEM has a direct impact on the derived slope value, hence DEM resolution greatly matters (Chang & Tsai, 1991). The focus of the analysis is on the change of slope values along the DEM transect due to changing DEM resolutions. Statistics of the slope transects are shown in Table 4. As the resolution of the DEM decreases (from 5 to 200 m pixel size), the average, maximum, standard deviation, and variance of the slope decrease. A decreasing slope average from lower resolution DEMs has been observed in previous studies (e.g., Chang & Tsai, 1991; Evans, 1980; Kienzle, 2004) and is well documented. The results here support these previous studies and reconfirm the relationship between DEM resolution and derived slope values.

The slope values implemented in PyFLOWGO depend also on the step size (i.e., which effectively resamples the downflow slopes) so they are not always identical to the slope values derived from the topographic profile (see section 4.2). The resampled slope values nonetheless follow the same trend as DEM resolution decreases.

Table 4. Slope statistics from the channel transect for the eight DEM resolutions.

	5 m DEM Slope	10 m DEM Slope	15 m DEM Slope	20 m DEM Slope	30 m DEM Slope	50 m DEM Slope	100 m DEM Slope	200 m DEM Slope
Data Points (count)	3272	1640	1097	824	553	335	169	89
Average Slope (°)	11.4	11.4	7.70	7.01	6.39	5.91	5.60	5.60
Median Slope (°)	10.3	10.5	7.23	6.63	6.00	5.52	5.34	5.49
Minimum Slope (°)	1.19	3.03	1.16	0.69	1.00	1.49	2.20	2.43
Maximum Slope (°)	55.1	50.9	31.0	24.1	17.9	13.1	11.4	10.1
Standard Deviation (°)	6.07	5.09	3.65	3.27	2.87	2.41	2.01	1.87
Variance (°)	36.8	25.9	13.3	10.7	8.21	5.78	4.03	3.44

The distribution of slope values for each transect is a right skewed distribution (Figure 2a). For the 15 m and lower resolution DEMs, as the DEM resolution decreases, the proportion of higher slope values (>10°) significantly decreases (Figure 2b). These higher slope values are averaged out as the DEM resolution decreases, whereas the proportion of moderate slope (≤10° and ≥2°) values increases. As DEM resolution decreases, moderate resolution slopes become dominant. This indicates that the higher slope values cover a proportionally smaller part of the downslope transect than the moderate values. This trend is also reflected in the decreasing average slope values (Table 4). In the transect used for this study, there is not a consistent relationship between the proportion of moderate slopes and DEM resolution when considering the full range of DEM resolutions.

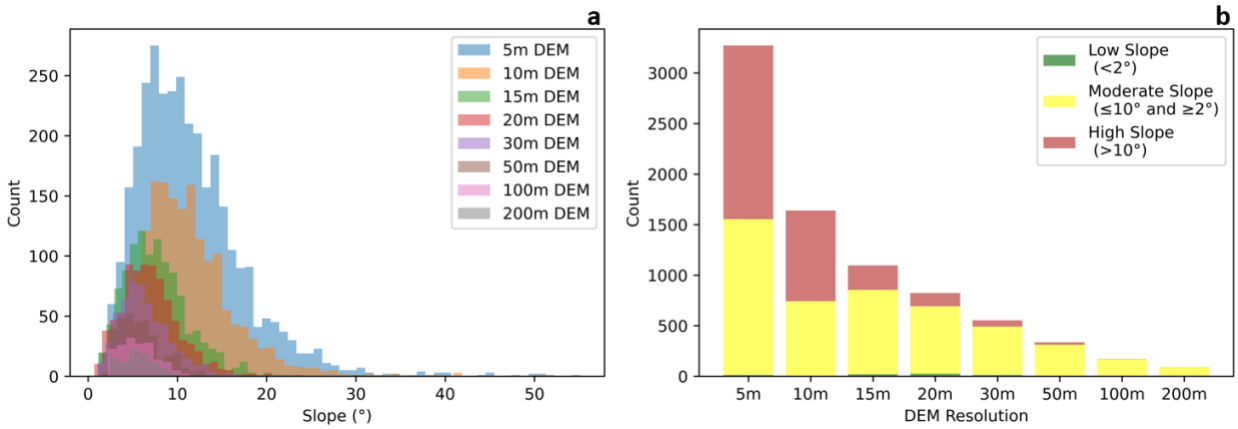

Figure 2. (a) Distribution of DEM slope values for the eight DEM resolutions. (b) Slope values distributed into three groups of low (<2°), moderate (≤10° and ≥2°), and high (>10°) values. Low slope (<2°) values are so few that they do not appear on the graph.

4.2 Convergence Analysis

A convergence analysis was used to assess the impact of step size in relation to the DEM resolution. Figure 3 shows how the final core temperature (K) and the final channelized flow distance (km) vary with changing step size in the model.

As the step size decreases, the final core temperature generally decreases, stabilizing for a step size of 5 m to 10 m. The final channelized flow length stabilizes at a step size of 10 m and below for the DEM resolutions of 5 m, 15 m, and 30 m. However, for the 200 m and constant slope a step size of 15 m can be used without significantly impacting the modeled channel length. Note that the final channelized flow length does vary with DEM resolution (being higher for the 200 m DEM than for the <30 m DEM) and will be discussed in section 4.3. The convergence analyses for core temperature and channel length is consistent with Chevrel et al. (2018) that in most cases a step size of 10 m or less is preferred to ensure stabilization of the model. If a future study is focused on core temperature, then a smaller step size may be needed. This may also be true for other parameters (i.e., viscosity, crystal fraction, yield strength) and highlights the need for a convergence analysis for any output parameter of interest. Other lava flow models that incorporate a step size (i.e., MAGFLOW) have also determined a step size between 5 m and 10 m is optimal (Bilotta et al., 2019). However, the smaller the step size, the longer the computation time, which is also a function of the length of the lava flow modeled. If rapid results for hazard response are required, the choice of step size may be a necessary consideration.

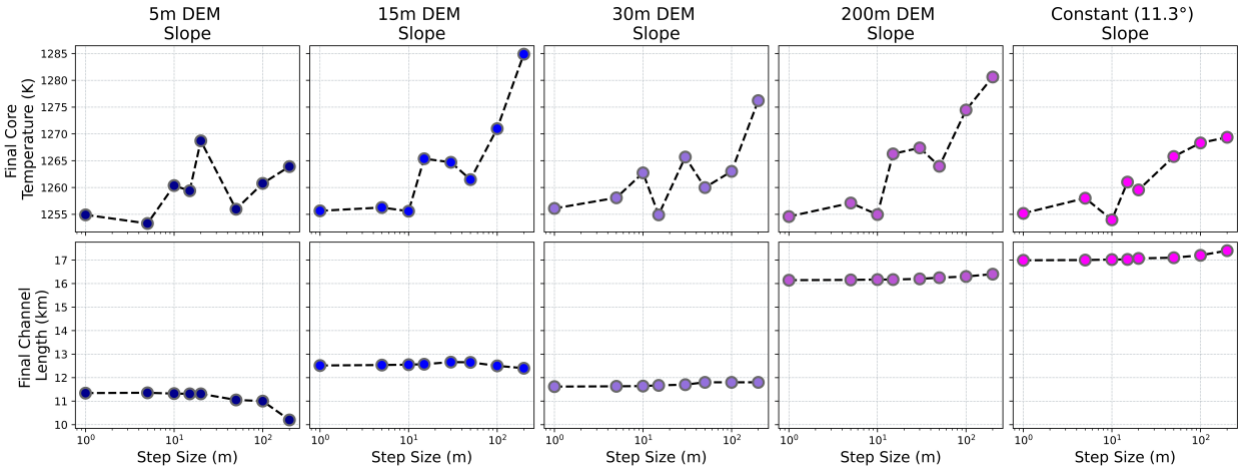

Figure 3. Convergence of the PyFLOWGO runs at 1, 5, 10, 15, 30, 50, 100, 200 m step size for the four different DEM derived slopes and the one constant slope (11.3°). The final channel length (bottom row) represents the distance the flow traveled once the velocity reaches zero.

If the step size is smaller than the resolution of the DEM, the model interpolates a profile between the two points and calculates slope values for each step. If the model step size is larger than the DEM resolution, the model averages over the slope values inside the step. Therefore, the amount of topographic variability can also impact the choice of step size. If there is little topographic variability (i.e., a smooth plain), then a larger step size could be used with potentially minor impact on the model. However, if the topography is highly variable (i.e., valleys, obstacles, etc.) then a smaller step size is required. To accurately and fully account for the topography present in a transect, a step size equal to or smaller than the DEM resolution should be used. To allow for a uniform comparison for the remainder of this manuscript, results using a 5 m step size are presented for all DEM resolutions examined.

4.3 Modeled Channel Length

We define the baseline model using the pre-flow 5 m DEM and all rheological model inputs from Ramsey et al. (2019), excluding the variable emissivity module as discussed in the Supplemental Material. To initialize the model and match the observed flow length of 11.3 km, Ramsey et al. (2019) used an ASTER-derived 30 m DEM and an effusion rate of 278 m^3/s. This initial effusion rate was taken from an estimation of the time averaged discharge rate (TADR)

obtained by the Middle Infrared Observation of Volcanic Activity (MIROVA) system (Coppola et al., 2016). Here, using the new pre-flow 5 m DEM and variable emissivity module, we obtained the desired channel length of 11.3 km for an effusion rate of 395 m^3/s. This value is slightly above the estimation from MIROVA but is reasonable as it falls in the range determined for the early phase of the eruption via field observations (aerial surveys) (440 m^3/s), the MIROVA system (278 m^3/s), and the TanDEM-X satellite (417 m^3/s) (Dvigalo et al., 2013; Kubanek et al., 2017; Ramsey et al., 2019). The effusion rate of 395 m^3/s is closer to the values of ~400 m^3/s or more determined by TanDEM-X and aero-photogrammetric observations that occurred during the first few days of the eruption.

Varying the resolution of the DEM, all simulated flows traveled farther than the simulation on the 5 m DEM for the same effusion rate (Figure 4). The simulation using the 10 m DEM resulted in a 12.8 km flow (12% increase); the 15 m DEM resulted in a 12.5 km flow (10% increase); the 20 m DEM resulted in a 12.4 km flow (9% increase); the 30 m DEM resulted in a 11.6 km flow (3% increase); the 50 m DEM resulted in a 11.5 km flow (1% increase); the 100 m DEM resulted in a 13.1 km flow (14% increase); and the 200 m DEM resulted in a 16.2 km flow (35% increase). The simulation on the constant slope the flow reached 17.0 km (40% increase) (Figure 4). All model runs stopped because the flow velocity reached zero. Good model fits (<5% increase in flow length) were obtained with the 5 m (baseline model), 30 m and 50 m DEMs. The 10 m, 15 m, 20 m, 100 m, 200 m, and constant slope had worse fits compared to the baseline model. Based on the slope statistics in Table 4, specifically the decreasing trend in average slope values with decreasing DEM resolution, the non-regular relationship between DEM resolution and modeled channel length was not expected. Analyses of slope values at Tolbachik (Figure 2b) show that the proportions of low, moderate, and high slopes do not systematically change with decreasing DEM resolution and may have an effect on modeled channel length.

4.4 Effusion Rate Variations

Effusion rate is one input for PyFLOWGO (or any lava flow model) that greatly influences lava flow length but is subject to large uncertainty (Harris et al., 2007; Rowland et al., 2005). An effusion rate is typically calculated indirectly from satellite thermal data, or directly from observations made in the field, and used in the model to match a defined channel/flow length or area. To assess the relationship between effusion rate and the resolution of the DEM, PyFLOWGO was run iteratively with different effusion rates for all seven DEM resolutions plus the constant

slope to match the 11.3 km channel length (Figure 5). All other input parameters remained constant, including the 5 m step size, for all DEM resolutions. The 5 m DEM is the baseline model as defined in section 4.3.

Figure 5 shows results for effusion rates for the eight DEM resolutions; these follow a non-regular trend, similar to the channel length results shown in Figure 4. Effusion rates similar to the baseline model at Tolbachik were found for the 30 and 50 m DEMs, whereas significantly lower values for the 10 m, 15 m, 30 m, 100 m and 200 m DEMs are needed to match the final channel length. This pattern is attributed to the decrease in topographic variability of the Tolbachik slope transect (Table 4 and Figure 2). For a low-resolution DEM (100 m and 200 m) or constant slope, there is substantially less topographic variability expressed in the transect. A markedly smaller effusion rate is necessary to reach the 11.3 km distance. With less topographic variability influencing the modeled flow, a lower effusion rate can therefore produce a lava flow of the same length. This could potentially lead to an underestimation of the effusion rate when using the model with lower resolution DEMs (e.g., ≥100 m) to determine a flow's emplacement conditions.

For many terrestrial volcanic eruptions, effusion rates spike early then follows an exponential decay (e.g., Bonny et al., 2018; Harris et al., 2000; Ramsey et al., 2019; Wadge, 1981; Wright et al., 2001). Most channelized lava flows are formed during this early period in the eruption (Rowland et al., 2005). The average initial effusion rate determined for 27 - 29 November 2012 from field observations at Tolbachik (i.e., aerial surveys) was ~400 m^3/s (Dvigalo et al., 2014; Kubanek et al., 2017). The observed flow length of 11.3 km occurred on 1 December 2012, early in the eruption. Using the higher resolution topographic data required a higher effusion rate to reach the same distance (Figure 5). In other words, the estimate of the effusion rate that produced a given flow should improve with higher resolution topography.

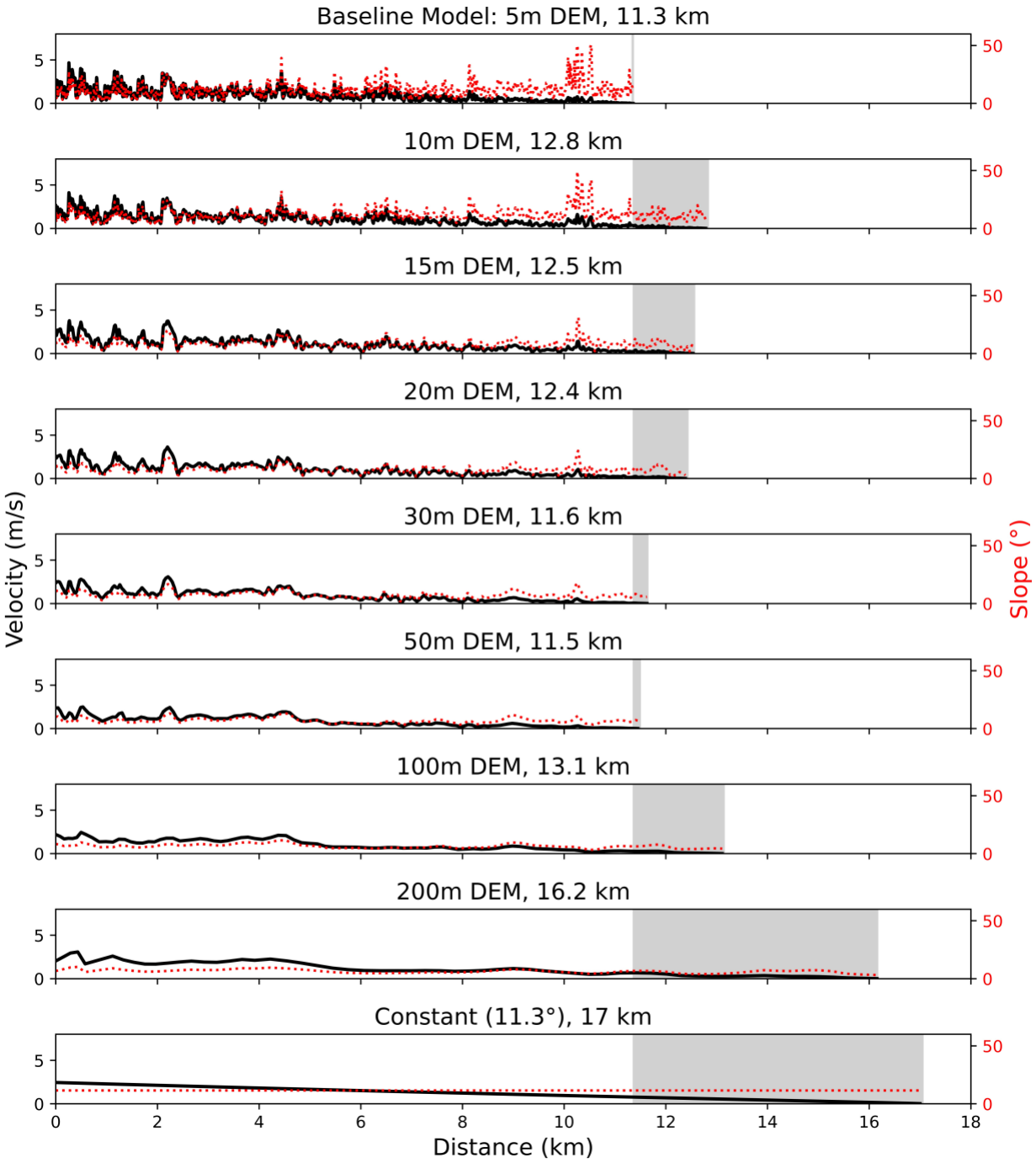

Figure 4. Model runout distances at a constant effusion rate (395 m^3/s) for eight DEM resolutions, and a constant slope. The black line represents lava velocity in the channel as a function of distance from the source. The red dotted line is the slope profile. The grey vertical line in the baseline model plot is the 11.3 km flow length observed on 1 December 2012, and the grey regions indicate the difference between the flow length of baseline model and the relevant model case. All model results shown here used a 5 m step size.

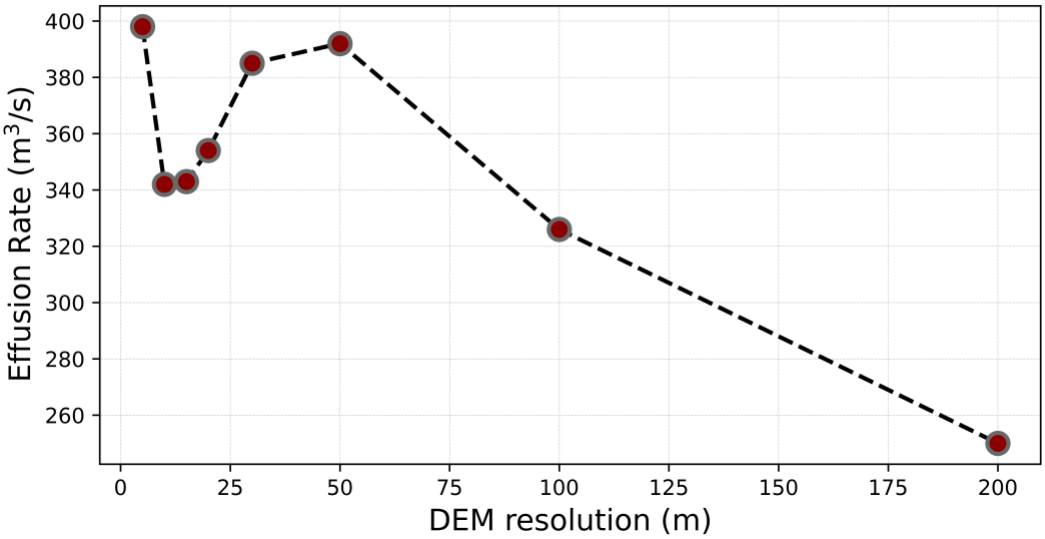

Figure 5. Required effusion rates as a function of DEM resolution to reach the 11.3 km channel length for the 5 m (395 m^3/s), 10 m (341 m^3/s), 15 m (342 m^3/s), 20 m (353 m^3/s), 30 m (384 m^3/s), 50 m (391 m^3/s), 100 m (325 m^3/s) and 200 m (249 m^3/s) model runs, and for the constant slope (11.3°) (248 m^3/s). All model results shown here used a 5 m step size.

4.5 PyFLOWGO Velocity

PyFLOWGO accounts for the change in topography through a modified version of Jeffreys equation to determine the flow velocity (Moore, 1987). To assess the lack of consistent channel length and effusion rate trend with decreasing DEM resolution observed in Figure 4 and 5, we next divided each modeled flow into three segments (proximal, medial, and distal) to compare changes in flow velocity as a result of the DEM resolution in those segments (Table 5). This was intended to explore how the distribution of slopes downflow might affect model results for different DEM resolutions as the higher slopes are reduced/smoothed in lower resolution DEMs. Proximal represents the first 10% of the channel length, medial the middle 65%, and distal the final 25%. These percentages are similar to those used for terrestrial and Martian lava flows in prior studies (Garry et al., 2007; Peitersen & Crown, 1999). The constant slope model run is not assessed because variations in topography are not present.

Table 5: Average modeled velocity for the proximal, medial, and distal flow portions. The last two columns are the average and median flow velocity over the entire modeled channel length.

	Modeled Channel Velocity (m/s)				
DEM Resolution	**Proximal (first 10%)**	**Medial (middle 65%)**	**Distal (final 25%)**	**Average Over Channel Length**	**Median Over Channel Length**
5 m	1.68	1.07	0.27	0.92	0.76
10 m	1.87	1.12	0.34	0.99	0.89
15 m	1.95	1.12	0.30	0.99	0.85
20 m	1.88	1.09	0.25	0.96	0.85
30 m	1.69	1.01	0.25	0.88	0.72
50 m	1.55	0.96	0.23	0.83	0.61
100 m	1.75	1.08	0.22	0.93	0.74
200 m	2.30	1.22	0.24	1.08	0.91

There is a decrease in the average and median flow velocities for the 10 m to 50 m DEM resolutions (Table 5). The same trend is not fully observed in the proximal, medial, or distal regions. There is an increase in velocity in the 10, 15, and 20 m DEM results for the proximal, medial, average, and median relative to the 5 m DEM results. For the distal region, the increase is seen in the 10 and 15 m results and not for the 20 m DEM. These trends follow the lack of consistent relationships with DEM resolution for channel length and effusion rate and are attributed to the specific topographic characteristics of the Tolbachik slope transect that influences flow velocity.

The decrease in flow velocity is attributed to the change in topographic variability at different locations along the slope transect (Table 4 and Figure 4). The slope transect used for the modeling contained large topographic changes that take up a proportionally smaller area than do the small to moderate changes (Figure 2). As large topographic changes (and by extension large slopes) are lost in the lower resolution DEMs, the flow is unable to maintain the same velocity to allow it to reach the same length as those derived from using the higher resolution DEMs. For high to moderate resolution DEMs (10 to 50 m), the fewer large slope changes in the transect leads to a lower average flow velocity. However, for the low resolution DEMs (100 m and 200 m) and constant slope there is an increase in both flow length and velocity in comparison to the moderate resolution DEMs (Figure 4 and Table 5). With these lower resolution DEMs, the topography has

smoothed to the point where there is little to no variability left to influence the final length (Table 4 and Figure 2). Although there are not high slope values to increase velocity, there are also not the corresponding decreases in slope that reduce velocity. The lower resolution DEMs can maintain a higher velocity and thus a longer flow distance.

For the case shown here, topographic effects and the resulting changes in velocity of the modeled lava flow might be site specific to the Tolbachik volcanic complex. These results highlight the importance for future studies to examine the magnitude and distribution of slope elements at the scale of the DEM to assess how they may influence the modeling results.

5 Discussion

The resolution of the DEM used for PyFLOWGO modeling has a measurable impact on the resulting channel length. These findings differ from Harris et al. (2016) who used two different topographic datasets, a 30 m DEM from the SRTM and a 10 m DEM produced from LIDAR, to compare the effect of different DEM resolutions on the FLOWGO model for a channelized lava flow from the December 2010 eruption of Piton de la Fournaise (Harris et al., 2016). Their study found that there is little difference between the two resolutions but did not elaborate on the details, since the focus of the study was on comparing field measurements to model results and not a detailed topographic sensitivity analysis. Comparing the results here for only the 30 m and 10 m DEMs, the length difference is 1.16 km or 9.5%, a potentially significant difference for lava flow hazard assessments and maps.

The changes in topographic variability related to the DEM resolutions and the effect on the calculated velocity partially explains the trend in flow lengths (Figure 2, Figure 4, and Table 5). However, we cannot rule out the possibility that the trend in channel length may be impacted by specific aspects of the topography at Tolbachik. The slope profile used in the study shows large variations near the proximal and distal end of the flow (Figure 4). These variations in slope are not fully averaged out except in the 100 m and 200 m DEM (Figure 2). Previous studies have shown that changes in topography at different points along a flow's emplacement can impact the final flow length and morphology (Flynn et al., 2021; Gregg & Fink, 2000; Guest et al., 1987). Assessing how different unique combinations of topographic variability impact lava flows emplacement is outside the scope of this work but should be further investigated.

Results from the topographic sensitivity analysis indicate that using a higher resolution DEM requires a higher effusion rate to model the same channel length especially for regions with large pre flow slope variability. Moderate to low resolution DEMs will underestimate the modeled effusion rate in these same circumstances. The remainder of the discussion centers on the implications of using different DEM resolutions for modeling both active and inactive lava flows.

5.1 Active Flows

PyFLOWGO is increasingly used to make hazard assessments for new volcanic events within minutes to hours of an eruption occurring (Chevrel et al., 2022; Harris et al., 2019; Peltier et al., 2021, 2022). In these cases, lava flow composition (i.e., rheological parameters) is usually determined based on past eruptions at that volcano. The two remaining inputs needed for the model are the effusion rate and the topography. Effusion rate for active eruptions is commonly calculated from repeat visible, thermal, or radar satellite data (Harris et al., 2007 and methods described within). Common tools for determining effusion rates from satellite data are the MIROVA (Coppola et al., 2016), HOTVOLC (Gouhier et al., 2016), and HOTSAT (Ganci et al., 2011) monitoring systems and data from the TanDEM-X satellite (Kubanek et al., 2021). Our results indicate that using the highest resolution DEM available, with an effusion rate from early in the eruption, produces the best fit to the observed channel length (provided the model is calibrated to that DEM resolution and chosen model step size as we show here). In an ideal situation, a high-resolution topographic dataset (i.e., 10 m DEM or better) is available coupled with effusion rate measurements made as soon as possible at the start of the eruption. However, if a study uses a moderate resolution DEM in combination with PyFLOWGO, an overestimate of the final channel length is possible depending on the pre-flow topography.

For some volcanoes (e.g., Etna, Kīlauea, Piton de la Fournaise), a 5 m (or better) DEM may be available. However, for many other volcanoes, especially those in remote locations, high resolution DEMs are not readily available or feasible to acquire. In those cases, a moderate resolution DEM (i.e., 30 m), such as the SRTM DEM or ASTER global DEM (GDEM) are freely available and provide global coverage. However, the SRTM DEM provides a snapshot of topography from February 2000, potentially missing important topographic changes since that time (van Zyl, 2001). In contrast, version 3 of the ASTER GDEM is more current, but averages together ASTER individual scene DEMs from 2000-2011. Averaging scenes together for the GDEM does produce a more accurate DEM, devoid of clouds and other errors, but it also averages

any topographic change during that period. Alternatively, an ASTER individual scene DEM (30 m/pixel) could be used. However, as highlighted in Flynn & Ramsey (2020), these scenes can contain substantial amounts of noise or interference from clouds and shadowing, despite being more representative of recent topographic change.

The impact of noise (and/or rapidly changing topography) in a DEM could be reduced using the "slope smoothing" function in PyFLOWGO. This function interpolates a line over the DEM based on a set number of points, defined by an individual before the model starts. It is important to note that, although using this function may reduce noise in a transect, it also removes naturally occurring topographic features smaller than the smoothing function. As highlighted in Harris et al. (2019) and Chevrel et al. (2022), calibration of PyFLOWGO for a given DEM resolution and step size is mandatory before using it for any hazard assessment. This ensures that the modeled lava flow distance for a given effusion rate is as accurate as possible.

5.2 Inactive Flows

PyFLOWGO can also be used to investigate the evolution of the thermorheological properties of already emplaced/inactive flows on Earth and other planetary bodies (cf. Table 2) (e.g., Lev et al., 2021; Ramsey et al., 2019; Rowland et al., 2004). Morphological parameters of terrestrial lava flows and rheological properties of the lava can be established through field campaigns and sample analysis, respectively. However, for flows on other planetary bodies, rheological conditions typically are assumed using an Earth analog or modeling (Chevrel et al., 2014). As discussed in Section 1, DEM resolution is limited for other planetary bodies, and pre-flow topography has not been available. Therefore, post-emplacement topography is assumed to be a suitable proxy.

Comparing the results for the 200 m DEM (the same resolution as the MOLA/HRSC global DEM for Mars) to the results for the constant slope, the modeled channel length difference is 850 m (5%). This is a potentially significant difference where attempting to reproduce very long (e.g., 100s of km) channelized lava flows observed on Mars or Venus. However, the difference in effusion rate required to model a given flow using the 200 m DEM and constant slope scenarios is negligible 0.4% (Figure 5). In order to apply PyFLOWGO to planetary lava flows the use of lower resolution DEMs or a constant slope is commonly required and will introduce uncertainty into the results. Results presented here quantify that uncertainty, which can aid future applications to planetary lava flows.

A potentially important factor typically overlooked in studies that use a constant slope for lava flow modeling is the value chosen. As shown in Table 4, as the resolution of the DEM decreases the average slope value also decreases and becomes less representative of the local topography. Figure 6 shows that the change in measured slope value relates to the resolution of the topographic dataset using data commonly available on Mars (i.e., a CTX and MOLA/HRSC DEM).

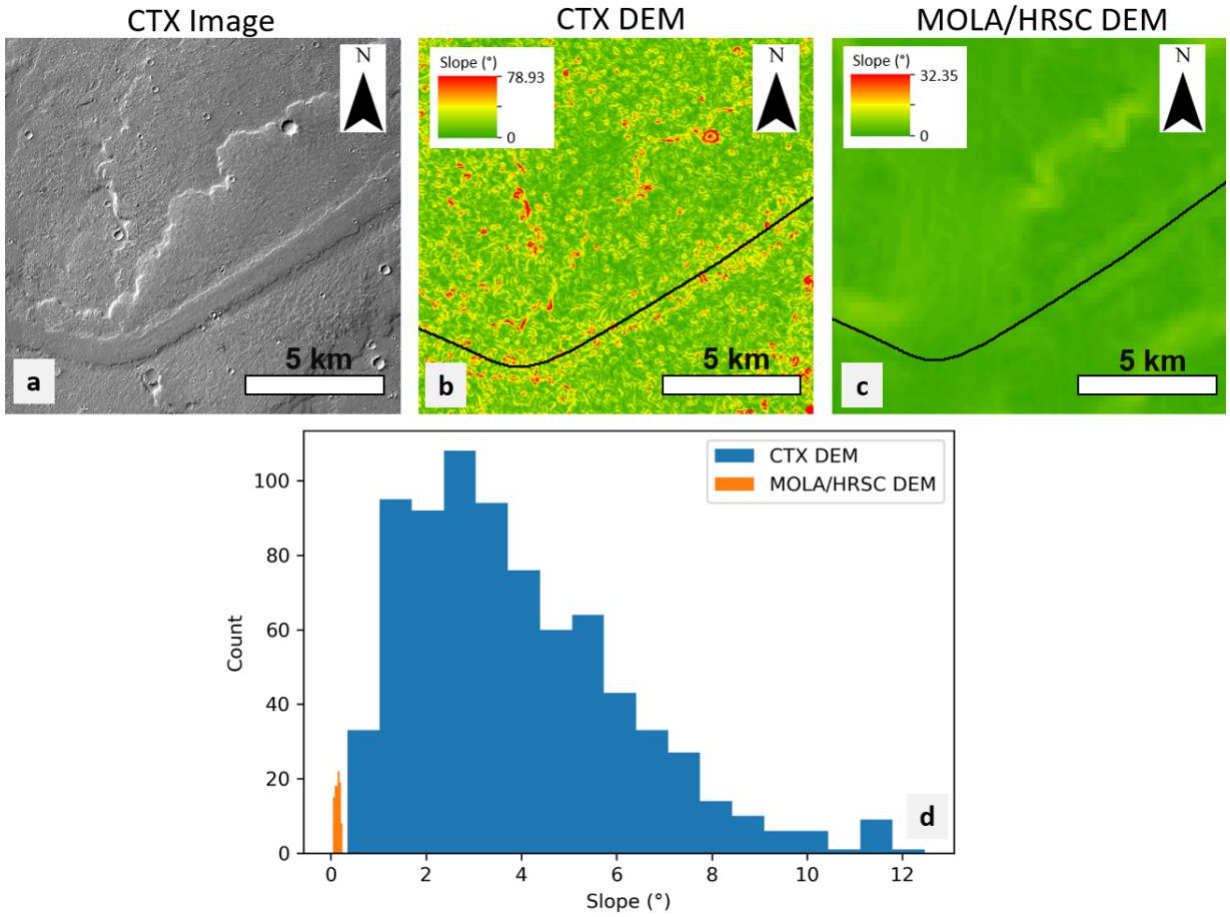

Figure 6: (a) A CTX image (P02_001775_1593) of a channelized lava flow located south of Arsia Mons, Mars. The central channel has been filled with a secondary lava flow, which distinctly outlines its path. (b) CTX slope map of the same location in (a) and the black line indicating the location of the central channel. (c) MOLA/HRSC slope map, derived from the MOLA/HRSC DEM. (d) Histogram distribution of slope values along the black line in (b) and (c). The average value for the CTX and MOLA/HRSC slope transects were 3.92° and 0.14°, respectively.

Previous modeling of Martian lava flows has used a constant slope (i.e., the standard rheologic approach described in Hiesinger et al., 2007). This value is usually derived from HRSC or MOLA data (e.g., Hiesinger et al., 2007; Pasckert et al., 2012; Peters et al., 2021). As shown in Table 4, Figure 2, and Figure 6, the higher resolution DEMs can provide a large range of slope values dependent on the resolution of the topographic dataset. This range in slope values can have a quantifiable effect on modeling results for effusion rate, viscosity, and yield strength (Russo et al., 2022). However, using a constant slope derived from the regional topography may be the best option if no pre-flow topography is available.

To assess the effects of the constant slope values we perform an additional model run using the average slope value derived from the 200 m DEM (5.6°) (Table 4). We compare the 5.6° constant slope model run to those from the 11.3° constant slope results. Our results show that the differences between a simulation on a constant slope of 5.6° or 11.3° is only 960 m (5%). Given the large (nearly two times) difference in average slope value, this is a relatively minor difference in distance. Although using a constant slope for lava flow modeling is not optimal, given the limitations of planetary datasets, errors related to this approximation are acceptable for a first order estimation of the lava flow emplacement dynamics.

6 Conclusions

The main objective of this work was to investigate the effect of DEM resolution on PyFLOWGO modeling. We used the 11.3 km-long lava flow emplaced during the Tolbachik 2012-2013 eruption as a reference and the same PyFLOWGO rheologic input parameters as provided by Ramsey et al. (2019) with the exception of the emissivity model for that same flow. Our approach consisted of comparing PyFLOWGO results on DEMs of decreasing resolution (from 5 m to 200 m).

Using a convergence analysis, we emphasize the importance of choosing an appropriate model step size to account for topography. In agreement with Chevrel et al. (2018) we show that a step size of 10 m or smaller should be used for a DEM with resolutions between 5 and 200 m. Choosing an appropriate model step size in relation to the DEM resolution is a necessary step to ensure accurate model results.

The topographic sensitivity analysis results indicate that DEM resolution is an important parameter to consider with PyFLOWGO. Using a moderate to low resolution (~10 m to ~200 m) DEM overestimates the channelized flow length, as does using a constant slope equal to the

549 average slope value. In addition, assessing the level of topographic variability in a modeled lava
550 flows path is an important consideration. This information supports the fact that regardless of the
551 level of complexity in a lava flow model, topography and its accuracy are critical parameters.
552 Studies using PyFLOWGO for active lava flow emplacement should strive to use the most recent
553 pre-flow DEM, especially for cases where the topography is frequently changing. If moderate to
554 low resolution DEMs are the only available options, either the effusion rate will be underestimated,
555 or the final channel length overestimated. However, where applying PyFLOWGO to inactive lava
556 flows (on Earth or other planetary bodies), a moderate to low resolution DEM may be the only
557 option. Interpreting these model results should be done with the expectation of higher error rates
558 in either the effusion rate or modeled channel length.

559 With the wide range of applications for PyFLOWGO, across multiple planetary bodies,
560 understanding the impact of topographic datasets resolution is important for accurate modeling
561 results. The topographic sensitivity analysis presented here provides useful information that can
562 be used to improve the application of PyFLOWGO for hazard assessments and investigation into
563 the emplacement of channelized flows on Earth and other planetary bodies.
564

565 **Acknowledgments and Data Availability Statement**

566 This research was supported through the NASA Solar System Workings (SSW) program (grant
567 number: 80NSSC19K0547). The authors would like to thank Dave Hyman and an anonymous
568 reviewer for their insightful reviews. The authors would also like to thank Andy Harris for
569 constructive input regarding FLOWGO. Thank you to Viktor Dvigalo and Alexander Belousov
570 for providing the Tolbachik DEM and to Dan Berman for generating the CTX DEM. All Planet
571 data were supplied through their Education and Research program. The PyFLOWGO model is
572 available for download at https://github.com/pyflowgo. PyFLOWGO results can be found at Flynn
573 (2023). This is a Laboratory of Excellence ClerVolc contribution no°594.

574 **References**

575 Baloga, S. M., & Glaze, L. S. (2008). A self-replication model for long channelized lava flows
576 on the Mars plains. *Journal of Geophysical Research E: Planets*, *113*(5), 1–15.
577 https://doi.org/10.1029/2007JE002954
578 Belousov, A., & Belousova, M. (2017). Dynamics and viscosity of ‘a’a and pahoehoe lava flows
579 of the 2012–2013 eruption of Tolbachik volcano, Kamchatka (Russia). *Bulletin of*
580 *Volcanology*, *80*(1). https://doi.org/10.1007/s00445-017-1180-2

Belousov, A., Belousova, M., Edwards, B., Volynets, A., & Melnikov, D. (2015). Overview of the precursors and dynamics of the 2012-13 basaltic fissure eruption of Tolbachik Volcano, Kamchatka, Russia. *Journal of Volcanology and Geothermal Research*, *307*, 22–37. https://doi.org/10.1016/j.jvolgeores.2015.06.013

Bilotta, G., Cappello, A., Hérault, A., & Del Negro, C. (2019). Influence of topographic data uncertainties and model resolution on the numerical simulation of lava flows. *Environmental Modelling and Software*, *112*(November 2018), 1–15. https://doi.org/10.1016/j.envsoft.2018.11.001

Bonny, E., Thordarson, T., Wright, R., Höskuldsson, A., & Jónsdóttir, I. (2018). The Volume of Lava Erupted During the 2014 to 2015 Eruption at Holuhraun, Iceland: A Comparison Between Satellite- and Ground-Based Measurements. *Journal of Geophysical Research: Solid Earth*, *123*(7), 5412–5426. https://doi.org/10.1029/2017JB015008

Breton, S., Quantin-Nataf, C., Bodin, T., Loizeau, D., Volat, M., & Lozac'h, L. (2019). Semi-automated crater depth measurements. *MethodsX*, *6*(May), 2293–2304. https://doi.org/10.1016/j.mex.2019.08.007

Chang, K. T., & Tsai, B. W. (1991). The effect of dem resolution on slope and aspect mapping. *Cartography and Geographic Information Systems*, *18*(1), 69–77. https://doi.org/10.1559/152304091783805626

Chevrel, M. O., Baratoux, D., Hess, K. U., & Dingwell, D. B. (2014). Viscous flow behavior of tholeiitic and alkaline Fe-rich martian basalts. *Geochimica et Cosmochimica Acta*, *124*, 348–365. https://doi.org/10.1016/j.gca.2013.08.026

Chevrel, M. O., Labroquere, J., Harris, A. J. L., & Rowland, S. K. (2018). PyFLOWGO : An open-source platform for simulation of channelized lava 25cience-rheological properties, *111*(November 2017), 167–180. https://doi.org/10.1016/j.cageo.2017.11.009

Chevrel, M. O., Favalli, M., Villeneuve, N., Harris, A. J. L., Fornaciai, A., Richter, N., et al. (2021). Lava flow hazard map of Piton de la Fournaise volcano. *Natural Hazards and Earth System Sciences*, *21*(8), 2355–2377. https://doi.org/10.5194/nhess-21-2355-2021

Chevrel, M. O., Harris, A., Peltier, A., Villeneuve, N., Coppola, D., Gouhier, M., & Drenne, S. (2022). Volcanic crisis management supported by near real-time lava flow hazard assessment at Piton de la Fournaise, La Réunion. *Volcanica*, *5*(2), 313–334. https://doi.org/10.30909/vol.05.02.313334

Churikova, T. G., Gordeychik, B. N., Edwards, B. R., Ponomareva, V. v., & Zelenin, E. A. (2015). The Tolbachik volcanic massif: A review of the petrology, volcanology and eruption history prior to the 2012-2013 eruption. *Journal of Volcanology and Geothermal Research*, *307*, 3–21. https://doi.org/10.1016/j.jvolgeores.2015.10.016

Coppola, D., Laiolo, M., Cigolini, C., Donne, D. D., & Ripepe, M. (2016). Enhanced volcanic hot-spot detection using MODIS IR data: results from the MIROVA system. *Geological Society, London, Special Publications*, *426*(1), 181–205. https://doi.org/10.1144/SP426.5

Dietterich, H. R., & Cashman, K. V. (2014). Channel networks within lava flows: Formation, evolution, and implications for flow behavior. *Journal of Geophysical Research: Earth Surface*, *119*, 1704–1724. https://doi.org/10.1002/2013JF002871.

Dvigalo, V. N., Svirid, I. Yu., & Shevchenko, A. V. (2014). The first quantitative estimates of parameters for the tolbachik fissure eruption of 2012-2013 from aerophotogrammetric observations. *Journal of Volcanology and Seismology*, *8*(5), 261–268. https://doi.org/10.1134/S0742046314050029

Evans, I. S. (1980). An integrated system of terrain analysis and slope mapping. *Zeitschrift Fur Geomorphologie*, *36*, 274–295.

Farr, T. G., Rosen, P. A., Caro, E., Crippen, R., Duren, R., Hensley, S., et al. (2007). The shuttle radar topography mission. *Reviews of Geophysics*, *45*(2).

Favalli, M., Pareschi, M. T., Neri, A., & Isola, I. (2005). Forecasting lava flow paths by a stochastic approach. *Geophysical Research Letters*, *32*(3), 1–4. https://doi.org/10.1029/2004GL021718

Favalli, M., Tarquini, S., & Fornaciai, A. (2011). Downflow code and lidar technology for lava flow analysis and hazard assessment at mount etna. *Annals of Geophysics*, *54*(5), 552–566. https://doi.org/10.4401/ag-5339

Favalli, M., Tarquini, S., Papale, P., Fornaciai, A., & Boschi, E. (2012). Lava flow hazard and risk at Mt. Cameroon volcano. *Bulletin of Volcanology*, *74*(2), 423–439. https://doi.org/10.1007/s00445-011-0540-6

Fedotov, S. A., Flerov, G. B., & Chirkov, A. M. (1984). The 1975–1976 Large Tolbachik Fissure Eruption in Kamchatka. *26cience, Moscow (637 Pp.)*.

Fergason, R. L., Hare, T. M., & Laura, J. (2018). HRSC and MOLA blended digital elevation model at 200m v2, astrogeology PDS annex. *US Geological Survey*.

Flynn, Ian. T. W., Chevrel, Magdalena. O., & Ramsey, Michael. S. (2023). Adaptation of a thermorheological lava flow model for Venus conditions. *Journal of Geophysical Research: Planets*. https://doi.org/https://doi.org/10.1029/2022JE007710

Flynn, Ian. (2023). Data for: "The effects of DEM resolution on the PyFLOWGO thermorheological lava flow model" paper [Data set]. Zenodo. https://doi.org/10.5281/zenodo.8021357

Flynn, I. T. W., Crown, D. A., & Ramsey, M. S. (2022). Determining Emplacement Conditions and Vent Locations for Channelized Lava Flows Southwest of Arsia Mons. *Journal of Geophysical Research: Planets*, *127*(11). https://doi.org/10.1029/2022JE007467

Flynn, I T W., Crown, D. A., & Ramsey, M. S. (2021). The Effects of DEM Resolution on Planetary Thermo-Rheological Lava Flow Modeling. In *52nd Lunar and Planetary Science Conference* (p. 1305).

Flynn, Ian T.W., & Ramsey, M. S. (2020). Pyroclastic density current hazard assessment and modeling uncertainties for Fuego volcano, Guatemala. *Remote Sensing*, *12*(17). https://doi.org/10.3390/RS12172790

Ford, P. G., & Pettengill, G. H. (1992). Venus topography and kilometer-scale slopes. *Journal of Geophysical Research*, *97*(E8), 103–114. https://doi.org/10.1029/92je01085

Ganci, G., Vicari, A., Fortuna, L., & del Negro, C. (2011). The HOTSAT volcano monitoring system based on combined use of SEVIRI and MODIS multispectral data. *Annals of Geophysics*, *54*(5), 544–550. https://doi.org/10.4401/ag-5338

Ganci, G., Cappello, A., Bilotta, G., & Del Negro, C. (2020). How the variety of satellite remote sensing data over volcanoes can assist hazard monitoring efforts: The 2011 eruption of Nabro volcano. *Remote Sensing of Environment*, *236*(September 2019), 111426. https://doi.org/10.1016/j.rse.2019.111426

Garry, W. B., Zimbelman, J. R., & Gregg, T. K. P. (2007). Morphology and emplacement of a long channeled lava flow near Ascraeus Mons Volcano, Mars. *Journal of Geophysical Research E: Planets*, *112*(8), 1–21. https://doi.org/10.1029/2006JE002803

Ghuffar, S. (2018). DEM generation from multi satellite Planetscope imagery. *Remote Sensing*, *10*(9), 1–22. https://doi.org/10.3390/rs10091462

672 Glaze, L. S., & Baloga, S. M. (2007). Topographic variability on Mars: Implications for lava
673 flow modeling. *Journal of Geophysical Research E: Planets*, *112*(8), 1–9.
674 https://doi.org/10.1029/2006JE002879
675 Gouhier, M., Guéhenneux, Y., Labazuy, P., Cacault, P., Decriem, J., & Rivet, S. (2016).
676 HOTVOLC: A web-based monitoring system for volcanic hot spots. *Geological Society,*
677 *London, Special Publications*, *426*(1), 223–241.
678 Gregg, T. K. P., & Fink, J. H. (2000). A laboratory investigation into the effects of slope on lava
679 flow morphology. *Journal of Volcanology and Geothermal Research*, *96*(3–4), 145–159.
680 https://doi.org/10.1016/S0377-0273(99)00148-1
681 Guest, J. E., Kilburn, C. R. J., Pinkerton, H., & Duncan, A. M. (1987). The evolution of lava
682 flow-fields: observations of the 1981 and 1983 eruptions of Mount Etna, Sicily. *Bulletin of*
683 *Volcanology*, *49*(3), 527–540.
684 Harris, A, Murray, J. B., Aries, S. E., Davies, M. A., Flynn, L. P., Wooster, M. J., et al. (2000).
685 Effusion rate trends at Etna and Krafla and their implications for eruptive mechanisms.
686 *Journal of Volcanology and Geothermal Research*, *102*(3–4), 237–269.
687 https://doi.org/10.1016/S0377-0273(00)00190-6
688 Harris, A. J. L., Dehn, J., & Calvari, S. (2007). Lava effusion rate definition and measurement: A
689 review. *Bulletin of Volcanology*, *70*(1), 1–22. https://doi.org/10.1007/s00445-007-0120-y
690 Harris, Andrew, & Rowland, S. K. (2015). FLOWGO 2012, An Updated Framework for
691 Thermorheological Simulations of Channel-Contained Lava. *Hawaiian Volcanoes: From*
692 *Source to Surface, Geophysical Monograph Series*, *208*, 457–481.
693 Harris, Andrew, & Rowland, Scott. K. (2001). FLOWGO: a kinematic Thermo-rheological
694 model for lava cooling in a channel. *Bulletin of Volcanology*, *63*, 20–44.
695 Harris, Andrew, Favalli, M., Mazzarini, F., & Pareschi, M. T. (2007). Best-fit results from
696 application of a thermo-rheological model for channelized lava flow to high spatial
697 resolution morphological data. *Geophysical Research Letters*, *34*(1), 1–5.
698 https://doi.org/10.1029/2006GL028126
699 Harris, Andrew, Favalli, M., Wright, R., & Garbeil, H. (2011). Hazard assessment at Mount Etna
700 using a hybrid lava flow inundation model and satellite-based land classification. *Natural*
701 *Hazards*, *58*(3), 1001–1027. https://doi.org/10.1007/s11069-010-9709-0
702 Harris, Andrew, Rhéty, M., Gurioli, L., Villeneuve, N., & Paris, R. (2016). Simulating the
703 thermorheological evolution of channel-contained lava: FLOWGO and its implementation
704 in EXCEL. *Geological Society Special Publication*, *426*(1), 313–336.
705 https://doi.org/10.1144/SP426.9
706 Harris, Andrew, Chevrel, M., Coppola, D., Ramsey, M., Hrysiewicz, A., Thivet, S., et al. (2019).
707 Validation of an integrated satellite-data-driven response to an effusive crisis: the April–
708 May 2018 eruption of Piton de la Fournaise. *Annals of GeophysicsAnnals of Geophysics*,
709 *61*(Vol 61 (2018)). https://doi.org/10.4401/ag-7972
710 Harris, Andrew., Rowland, S., & Chevrel, M. O. (2022). The anatomy of a channel-fed ʻaʻā lava
711 fow system. *Bulletin of Volcanology*.
712 Herrick, R. R., Stahlke, D. L., & Sharpton, V. L. (2012). Fine-scale Venusian topography from
713 Magellan stereo data. *Eos*, *93*(12), 125–126. https://doi.org/10.1029/2012EO120002
714 Hiesinger, H., Head, J., & Neukum, G. (2007). Young lava flows on the eastern flank of
715 Ascraeus Mons: Rheological properties derived from High Resolution Stereo
716 Camera(HRSC) images and Mars Orbiter Laser Altimeter(MOLA) data. *Journal of*
717 *Geophysical Research E: Planets*, *112*(5). https://doi.org/10.1029/2006JE002717

718 Hirano, A., Welch, R., & Lang, H. (2003). Mapping from ASTER stereo image data: DEM
719 validation and accuracy assessment. *ISPRS Journal of Photogrammetry and Remote*
720 *Sensing*, *57*(5–6), 356–370. https://doi.org/10.1016/S0924-2716(02)00164-8
721 Jaumann, R., Neukum, G., Behnke, T., Duxbury, T. C., Eichentopf, K., Flohrer, J., et al. (2007).
722 The high-resolution stereo camera (HRSC) experiment on Mars Express: Instrument aspects
723 and experiment conduct from interplanetary cruise through the nominal mission. *Planetary*
724 *and Space Science*, *55*(7–8), 928–952. https://doi.org/10.1016/j.pss.2006.12.003
725 Kienzle, S. (2004). The effect of DEM raster resolution on first order, second order and
726 compound terrain derivatives. *Transactions in GIS*, *8*(1), 83–111.
727 https://doi.org/10.1111/j.1467-9671.2004.00169.x
728 Kubanek, J., Richardson, J. A., Charbonnier, S. J., & Connor, L. J. (2015). Lava flow mapping
729 and volume calculations for the 2012–2013 Tolbachik, Kamchatka, fissure eruption using
730 bistatic TanDEM-X InSAR. *Bulletin of Volcanology*, *77*(12), 1–13.
731 https://doi.org/10.1007/s00445-015-0989-9
732 Kubanek, J., Westerhaus, M., & Heck, B. (2017). TanDEM-X Time Series Analysis Reveals
733 Lava Flow Volume and Effusion Rates of the 2012–2013 Tolbachik, Kamchatka Fissure
734 Eruption. *Journal of Geophysical Research: Solid Earth*, *122*(10), 7754–7774.
735 https://doi.org/10.1002/2017JB014309
736 Kubanek, J., Poland, M. P., & Biggs, J. (2021). Applications of bistatic radar to volcano
737 topography-a review of ten years of TanDEM-X. *IEEE Journal of Selected Topics in*
738 *Applied Earth Observations and Remote Sensing*, *14*, 3282–3302.
739 https://doi.org/10.1109/JSTARS.2021.3055653
740 Lee, R. J., & Ramsey, M. S. (2016). What is the emissivity of active basaltic lava flows.
741 *Proceedings of the AGU Fall Meeting, San Francisco, CA, USA*, 12–16.
742 Lev, E., Hamilton, C. W., Voigt, J. R. C., Stadermann, A. C., Zhan, Y., & Neish, C. D. (2021).
743 Emplacement conditions of lunar impact melt flows. *Icarus*, *369*(June).
744 https://doi.org/10.1016/j.icarus.2021.114578
745 Lipman, P. W., & Banks, N. (1987). A'a flow dynamics, 1984 Mauna Loa eruption. *Volcanism*
746 *in Hawaii*, (May), 43.
747 Moore, H. J. (1987). Preliminary estimates of the rheological properties of 1984 Mauna Loa
748 lava. *US Geol Surv Prof Pap*, *1350*(99), 1569–1588.
749 Mossoux, S., Saey, M., Bartolini, S., Poppe, S., Canters, F., & Kervyn, M. (2016). Q-LAVHA: A
750 flexible GIS plugin to simulate lava flows. *Computers and Geosciences*, *97*(September),
751 98–109. https://doi.org/10.1016/j.cageo.2016.09.003
752 Pasckert, J. H., Hiesinger, H., & Reiss, D. (2012). Rheologies and ages of lava flows on Elysium
753 Mons, Mars. *Icarus*, *219*(1), 443–457. https://doi.org/10.1016/j.icarus.2012.03.014
754 Peitersen, M., & Crown, D. A. (1999). Downflow width behavior of Martian and terrestrial lava
755 flows. *Journal of Geophysical Research*, *104*, 8473–8488.
756 Peltier, A., Ferrazzini, V., di Muro, A., Kowalski, P., Villeneuve, N., Richter, N., et al. (2021).
757 Volcano crisis management at Piton de la Fournaise (La Réunion) during the COVID-19
758 lockdown. *Seismological Society of America*, *92*(1), 38–52.
759 Peltier, A., Chevrel, M. O., Harris, A. J. L., & Villeneuve, N. (2022). Reappraisal of gap analysis
760 for effusive crises at Piton de la Fournaise. *Journal of Applied Volcanology*, *11*(1), 1–17.
761 https://doi.org/10.1186/s13617-021-00111-w

762 Peters, S. I., Christensen, P. R., & Clarke, A. B. (2021). Lava Flow Eruption Conditions in the
763 Tharsis Volcanic Province on Mars. *Journal of Geophysical Research: Planets*, *126*(7).
764 https://doi.org/10.1029/2020JE006791
765 Ramsey, M. S., Chevrel, M. O., Coppola, D., & Harris, A. J. L. (2019). The influence of
766 emissivity on the thermo-rheological modeling of the channelized lava flows at tolbachik
767 volcano. *Annals of Geophysics*, *62*(Special Issue), 44. https://doi.org/10.4401/ag-8077
768 Rhéty, M., Harris, A., Villeneuve, N., Gurioli, L., Médard, E., Chevrel, O., & Bachélery, P.
769 (2017). A comparison of cooling-limited and volume-limited flow systems: Examples from
770 channels in the Piton de la Fournaise April 2007 lava-flow field. *Geochemistry, Geophysics,*
771 *Geosystems*, *18*(9), 3270–3291. https://doi.org/10.1002/2017GC006839
772 Richardson, P., & Karlstrom, L. (2019). The multi-scale influence of topography on lava flow
773 morphology. *Bulletin of Volcanology*, *81*(4). https://doi.org/10.1007/s00445-019-1278-9
774 Riker, J. M., Cashman, K. V., Kauahikaua, J. P., & Montierth, C. M. (2009). The length of
775 channelized lava flows: Insight from the 1859 eruption of Mauna Loa Volcano, Hawai'i.
776 *Journal of Volcanology and Geothermal Research*, *183*(3–4), 139–156.
777 https://doi.org/10.1016/j.jvolgeores.2009.03.002
778 Rizzoli, P., Martone, M., Gonzalez, C., Wecklich, C., Borla Tridon, D., Bräutigam, B., et al.
779 (2017). Generation and performance assessment of the global TanDEM-X digital elevation
780 model. *ISPRS Journal of Photogrammetry and Remote Sensing*, *132*, 119–139.
781 https://doi.org/10.1016/j.isprsjprs.2017.08.008
782 Robert, B., Harris, A., Gurioli, L., Médard, E., Sehlke, A., & Whittington, A. (2014). Textural
783 and rheological evolution of basalt flowing down a lava channel. *Bulletin of Volcanology*,
784 *76*(6), 1–21. https://doi.org/10.1007/s00445-014-0824-8
785 Rowland, S. K., Harris, A. J. L., Wooster, M. J., Amelung, F., Garbeil, H., Wilson, L., &
786 Mouginis-Mark, P. J. (2003). Volumetric characteristics of lava flows from interferometric
787 radar and multispectral satellite data: The 1995 Fernandina and 1998 Cerro Azul eruptions
788 in the western Galápagos. *Bulletin of Volcanology*, *65*(5), 311–330.
789 https://doi.org/10.1007/s00445-002-0262-x
790 Rowland, S. K., Harris, A. J. L., & Garbeil, H. (2004). Effects of Martian conditions on
791 numerically modeled, cooling-limited, channelized lava flows. *Journal of Geophysical*
792 *Research E: Planets*, *109*(10), 1–16. https://doi.org/10.1029/2004JE002288
793 Rowland, S. K., Garbeil, H., & Harris, A. J. L. (2005). Lengths and hazards from channel-fed
794 lava flows on Mauna Loa, Hawai'i, determined from thermal and downslope modeling with
795 FLOWGO. *Bulletin of Volcanology*, *67*(7), 634–647. https://doi.org/10.1007/s00445-004-
796 0399-x
797 Russo, F. P., Flynn, I. T. W., & Ramsey, M. S. (2022). The Impact of Slope Variability on the
798 Modeling of Martian Lava Flows. *LPI Contributions*, *2678*, 1410.
799 Stefanescu, E. R., Bursik, M., & Patra, A. K. (2012). Effect of digital elevation model on Mohr-
800 Coulomb geophysical flow model output. *Natural Hazards*, *62*(2), 635–656.
801 https://doi.org/10.1007/s11069-012-0103-y
802 Sutton, S. S., Chojnacki, M., Mcewen, A. S., Kirk, R. L., Dundas, C. M., Schaefer, E. I., et al.
803 (2022). Revealing Active Mars with HiRISE Digital Terrain Models. *Remote Sensing*,
804 *14*(2403), 1–40.
805 Takaku, J., Tadono, T., Doutsu, M., Ohgushi, F., & Kai, H. (2020). Updates of aw3d30' alos
806 global digital surface model with other open access datasets. In *International Archives of*
807 *the Photogrammetry, Remote Sensing and Spatial Information Sciences - ISPRS Archives*

(Vol. 43, pp. 183–190). International Society for Photogrammetry and Remote Sensing. https://doi.org/10.5194/isprs-archives-XLIII-B4-2020-183-2020

Thompson, J. O., & Ramsey, M. S. (2021). The influence of variable emissivity on lava flow propagation modeling. *Bulletin of Volcanology*, *83*(6), 1–19. https://doi.org/10.1007/s00445-021-01462-3

Vetere, F., Rossi, S., Namur, O., Morgavi, D., Misiti, V., Mancinelli, P., et al. (2017). Experimental constraints on the rheology, eruption, and emplacement dynamics of analog lavas comparable to Mercury's northern volcanic plains. *Journal of Geophysical Research: Planets*, *122*(7), 1522–1538. https://doi.org/10.1002/2016JE005181

Wadge, G. (1981). The variation of magma discharge during basaltic eruptions. *Journal of Volcanology and Geothermal Research*, *11*(2), 139–168. https://doi.org/https://doi.org/10.1016/0377-0273(81)90020-2

Wantim, M. N., Kervyn, M., Ernst, G. G. J., del Marmol, M. A., Suh, C. E., & Jacobs, P. (2013). Numerical experiments on the dynamics of channelised lava flows at Mount Cameroon volcano with the FLOWGO thermo-rheological model. *Journal of Volcanology and Geothermal Research*, *253*, 35–53. https://doi.org/10.1016/j.jvolgeores.2012.12.003

Wright, R., Blake, S., Harris, A. J. L., & Rothery, D. A. (2001). A simple explanation for the space-based calculation of lava eruption rates. *Earth and Planetary Science Letters*, *192*(2), 223–233. https://doi.org/10.1016/S0012-821X(01)00443-5

Wright, R., Garbeil, H., & Harris, A. J. L. (2008). Using infrared satellite data to drive a thermo-rheological/stochastic lava flow emplacement model: A method for near-real-time volcanic hazard assessment. *Geophysical Research Letters*, *35*(19). https://doi.org/10.1029/2008GL035228

Zuber, M. T., Smith, D. E., Solomon, S. C., Muhleman, D. O., Head, J. W., Garvin, J. B., Abshire, J. B., & Bufton, J. L. (1992). The Mars Observer laser altimeter investigation. *Journal of Geophysical Research*, *97*(E5), 7781–7797. https://doi.org/10.1029/92JE00341

van Zyl, J. J. (2001). The Shuttle Radar Topography Mission (SRTM): a breakthrough in remote sensing of topography. *Acta Astronautica*, *48*(5–12), 559–565.

854

855 **Table 3.** PyFLOWGO input models, modules, and parameters that were used to simulate the 11.3 km channelized
856 Leningradskoye lava flow from 1 December 2012 (e.g., Ramsey et al., 2019). The * next to step size indicates that
857 this parameter was varied for a part of this study. For a full breakdown of abbreviations in the table see Chevrel et al.
858 (2018).

859

Models	**Selection**	**References**
Crystallization Rate	basic	Harris and Rowland (2001)
Melt Viscosity	vft	Giordano et al. 2008)
Relative Viscosity	er	Einstein-Roscoe model from Chevrel et al. (2018)
Yield Strength	ryerson	Ryerson et al. (1988)
Crust Temperature	constant	Harris and Rowland (2001)
Effective Crust Cover	basic	Harris and Rowland (2001)
Vesicle Fraction	constant	Harris and Rowland (2001)
Heat Budget Modules	**Selection**	**References**
Radiation	yes	Harris and Rowland (2001) and Ramsey et al. (2019)
Conduction	yes	Harris and Rowland (2001)
Convection	yes	Harris and Rowland (2001)
Rain	no	Harris and Rowland (2001)
Viscous Heating	no	Harris and Rowland (2001)
Initial Input Parameters	**Value**	**References**
Step Size*	10 m	Harris and Rowland (2001)
Effusion Rate*	278 - 400 m^3s^{-1}	MIROVA (this study)
Width	30 m	Ramsey et al. (2019)
Depth	6.1 m	Ramsey et al. (2019)
Gravity	9.81 ms^{-2}	

Eruption Temperature	1355.15 K	Plechov et al. (2015)
Crystal Fraction	25%	Plechov et al. (2015)
Dense Rock Equivalent Density	2630 kg m^3	Plechov et al. (2015)
Vesicle Fraction	0.06	Plechov et al. (2015)
Stefan-Boltzmann constant	5.60E-08	
Emissivity Crust	0.95	Ramsey et al. (2019)
Emissivity Uncrusted	0.6	Lee & Ramsey, (2016)
Basal Temperature	773.15 K	Harris and Rowland (2001)
Distance from Core to Base	19%	Harris and Rowland (2001)
Wind Speed	5 ms^{-1}	Harris and Rowland (2001)
Air Friction Factor	0.0036	Harris and Rowland (2001)
Air Temperautre	273.15 K	Harris and Rowland (2001)
Air Density	0.4412 kg m^{-3}	Harris and Rowland (2001)
Air Specific Heat Capacity	1099 J kg^{-1} K^{-1}	Harris and Rowland (2001)
Buffer	140 °C	Harris and Rowland (2001)
Crust Cover Fraction	0.9	Ramsey et al. (2019)
Velocity Dependency of Crust	-0.16	Ramsey et al. (2019)
Crust Temperature	773.15 K	Belousov et al. (2015)
a vft	-4.55 Pa s	Volynets et al. (2015)
b vft	6887.303 J mol^{-1}	Volynets et al. (2015)
c vft	527.44 K	Volynets et al. (2015)
Crystal Growth	0.37	Ramsey et al. (2019)
Solid Temperature	1253.15 K	Ramsey et al. (2019)
Latent heat of Crystallization	350000 K kg^{-1}	Harris and Rowland (2001)

860

861

862

863

864

865

866

867

868

869